

# The Importance of Accounting for Excited States in Ab Initio Modeling of Photocatalytic Mechanism: Insights from N<sub>2</sub> Reduction on a Ru–TiO<sub>2</sub> Cluster

Taja Žibert, Blaž Likozar,\* and Matej Huš\*

Photocatalytic nitrogen reduction is a sustainable alternative to the Haber–Bosch process, allowing ammonia production under mild conditions using light as the driving force for nitrogen fixation. Despite several experimental studies on photocatalytic ammonia synthesis, first-principles mechanistic studies are lacking, and only the ground state is typically considered. Herein, a multiscale model of photocatalytic ammonia synthesis is built, which is ab initio, explicitly accounts for excited states, and feeds into a coupled microkinetic model. Time-dependent density functional theory is employed to study the electronic properties of a Ru<sub>3</sub>–(TiO<sub>2</sub>)<sub>6</sub> cluster, its adsorption capabilities, and the reaction kinetics of ammonia synthesis in the ground state and the first excited state. The reaction parameters are then cast into a microkinetic model, which shows that the catalyst is active and elucidates the effect of varying reaction conditions on performance. Crucially, it is shown that without accounting for the excited states, the kinetics of the reaction are erroneously described. The reaction proceeds via a dissociative pathway, with N≡N bond cleavage as the rate-determining step. The apparent activation barrier in the excited state is decreased from 1.98 to 1.84 eV, increasing the reaction rate. This computational approach is transferable to other photocatalytic reactions.

which has traditionally been achieved via the thermocatalytic Haber–Bosch (HB) process. This process remains the dominant method for ammonia synthesis despite concerns regarding its environmental impact.<sup>[1,2]</sup> Ammonia is the second most widely produced chemical and is used as a fertilizer, an energy or hydrogen storage vector, and an intermediate for nitrogen-containing chemicals, such as platform chemicals, polymers, and explosives. Its use has also recently been recognized as a fuel in marine transportation.<sup>[1,2]</sup> During the HB process, considerable energy is required to achieve high temperatures and pressures necessary for nitrogen activation. Additionally, a notable carbon footprint is generated during hydrogen production, which is derived from methane via the methane steam reforming process. Consequently, there is growing interest in developing more environmentally friendly methods for ammonia synthesis, including photocatalysis.<sup>[3]</sup>

Photocatalysis is a sustainable alterna-

tive to the HB process, using a range of photocatalysts that have already been successfully deployed. These include titanium dioxide (TiO<sub>2</sub>), metal oxides, graphitic carbon nitrides (g-C<sub>3</sub>N<sub>4</sub>), bismuth oxyhalides (BiOX, X = Cl, Br), sulfides, and other photocatalysts.<sup>[4]</sup> Among them, TiO<sub>2</sub> is considered a benchmark catalyst due to its nontoxicity, high chemical stability, surface area, and photocatalytic activity, enabling its use in a wide range of applications in the cosmetic, pharmaceutical, and health industries, as well as a photocatalytic material.<sup>[5,6]</sup> It is used not only for photocatalytic N<sub>2</sub> fixation but also for water splitting,<sup>[7,8]</sup> CO<sub>2</sub> reduction,<sup>[5,9]</sup> and several other industrial reactions.

However, recent advances have disproportionately focused on experiments. Computational and theoretical work on modeling photocatalysis typically settles for computing some catalyst properties in the excited state, yet more often than not, only ground-state mechanisms are provided. In the latter case, calculations are performed over a selected photocatalyst in its ground state, without considering electron excitation. Few studies include time-dependent density functional theory calculations (TD-DFT),<sup>[10]</sup> while others use ab initio nonadiabatic molecular dynamics simulations (NAMMD),<sup>[11,12]</sup> Optical absorption of small (TiO<sub>2</sub>)<sub>n</sub>, n = 21–24 nanoparticles was studied in the framework of TD-DFT, which showed strong recombination of electron–hole


## 1. Introduction

Significant focus has been placed on the activation of a stable and inert nitrogen molecule and its reduction to ammonia,

T. Žibert, B. Likozar, M. Huš  
Department of Catalysis and Chemical Reaction Engineering  
National Institute of Chemistry  
Hajdrihova 19, SI-1001 Ljubljana, Slovenia  
E-mail: blaz.likozar@ki.si; matej.hus@ki.si

T. Žibert, M. Huš  
University of Nova Gorica  
Vipavska cesta 13, SI-5000 Nova Gorica, Slovenia

M. Huš  
Association for Technical Culture (ZOTKS)  
Zaloška 65, SI-1001 Ljubljana, Slovenia

 The ORCID identification number(s) for the author(s) of this article can be found under <https://doi.org/10.1002/sstr.202500221>.

© 2025 The Author(s). Small Structures published by Wiley-VCH GmbH. This is an open access article under the terms of the Creative Commons Attribution License, which permits use, distribution and reproduction in any medium, provided the original work is properly cited.

DOI: 10.1002/sstr.202500221

pairs obtained from the difference between the optical absorption onset and quasiparticle gaps.<sup>[10]</sup> Existing studies of photocatalytic ammonia production using first-principles modeling focused on  $N_2$  activation. NAMD calculations of the direct formation of the  $*N_2^-$  species on metal-free boron-decorated diamond clusters showed that the lifetime of the excited state of  $N_2$  (10 ns) is long enough to achieve the initial hydrogenation.<sup>[11]</sup> NAMD simulations were also used to study the photoactivation of  $N_2$  on a BiOBr photocatalyst with oxygen vacancies (OV). The formation of  $*N_2^-$  is stabilized by trapping the photogenerated electrons around the conduction band of the OV-BiOBr photocatalyst. Using the Hefei-NAMD approach, Niu et al.<sup>[12]</sup> modeled faster and lighter electrons with quantum mechanics and slower and heavier nuclei classically with ab initio MD. This approach is useful for performing ab initio NAMD.<sup>[13]</sup> Another approach is to study the trajectories of surface hopping with time-dependent Kohn–Sham equations.<sup>[14]</sup>

To the best of our knowledge, we perform the first full ab initio mechanistic study of nitrogen reduction under photocatalytic conditions in the excited state in this work. We combine TD-DFT calculations with microkinetic modeling to investigate photocatalytic ammonia synthesis over a  $Ru_3-(TiO_2)_6$  cluster photocatalyst, which is used due to the proven activity of Ru-doped  $TiO_2$  nanoparticles.<sup>[15–17]</sup> The initial determination of the thermodynamically most feasible structure of the  $Ru_3-(TiO_2)_6$  cluster is followed by an exploration of the electronic and optical properties that contribute to a better understanding of the behavior of the selected cluster as a photocatalytic material. We computed the band gap and projected densities of states. After determining the adsorption modes of the nitrogen molecule ( $N_2$ ), ammonia ( $NH_3$ ), and hydrogen (as H and  $H_2$ ), the overall nitrogen reduction mechanism was first studied in the ground state. Later, the reaction mechanism was studied in the first excited state using the TD-DFT method to account for the photocatalytic process. The obtained kinetic parameters (stemming from the adsorption energies and activation barriers for elementary reaction steps) were incorporated into a microkinetic model, which describes the reaction kinetics of the photocatalytic reduction mechanism as a function of reaction conditions. Most crucially, the approach is shown to be transferable to other heterogeneous photocatalytic reactions, making it a versatile tool for future theoretical photocatalysis research. In our study, we emphasize the importance of incorporating excited-state calculations into kinetic models. Rather than focusing on developing new formulations for photocatalysts, we aim to demonstrate that accounting for excited-state excitations in mechanistic studies is crucial, as it can significantly alter the reaction kinetics. To the best of our knowledge, a comprehensive microkinetic model that includes the excited-state surface has not yet been studied.

## 2. Methods

### 2.1. Ab Initio Calculations

Spin-polarized DFT and TD-DFT calculations were performed in the GPAW<sup>[18,19]</sup> environment and in the VASP software.<sup>[20,21]</sup> GPAW was implemented to study the electronic properties and charge transfer, while VASP was used to study the

adsorption/desorption equilibria and the nitrogen reduction mechanism in the ground and first excited states. To ensure consistency between GPAW and VASP, the same basis set, functional, convergence criteria, and other parameters were used. A plane-wave basis set was employed to describe wave functions within the projector augmented wave method as implemented in GPAW and VASP, respectively. A cutoff energy of 500 eV proved to be well converged for the system studied. The Perdew–Burke–Ernzerhof (PBE) functional<sup>[22]</sup> was used to obtain the adsorption energies and mechanism kinetics. To calculate the electronic properties more accurately, we applied the hybrid Heyd–Scuseria–Ernzerhof functional (HSE06)<sup>[23]</sup> as single-point calculations in the spin-polarized regime due to its high computational cost. The convergence criterion was set to 0.0005 eV per electron for energy and 0.01 eV  $\text{\AA}^{-1}$  for the forces on each atom. The  $Ru_3-(TiO_2)_6$  cluster photocatalyst was placed in a simulation cell large enough to ensure at least 10  $\text{\AA}$  of vacuum in each dimension. The simulation cell was sampled at a  $\Gamma$  point only to minimize spurious intercell interactions. All calculations were conducted using Fermi–Dirac smearing of 0.001 eV. To account for van der Waals interactions, the Grimme-D3 correction was applied.<sup>[24]</sup> To consider the on-site Coulomb interactions, a Hubbard-U correction of 4 eV was applied to the Ti 3d electrons<sup>[25–27]</sup> in the PBE approach.

#### 2.1.1. Catalyst Model

$TiO_2$  is recognized as a promising catalyst in ammonia synthesis due to its attractive properties, as outlined in the Introduction section. It crystallizes in different polymorphs (anatase, rutile, and brookite). Among them, rutile is thermodynamically the most stable, while anatase has been demonstrated to be a superior photocatalyst.<sup>[28]</sup> Clusters have proven to be effective catalysts for studying structure-related properties and determining active sites with greater accuracy compared to crystalline catalysts. This is due to the undercoordination of atoms in clusters.<sup>[29]</sup> In our previous study,<sup>[15]</sup> we investigated the structure-dependent properties of different pristine and ruthenium (Ru)-doped  $TiO_2$  clusters. Our findings revealed that smaller clusters exhibited higher reactivity toward nitrogen, while the presence of the Ru atom significantly improved electronic and adsorption properties. Based on these observations, we selected a medium-sized  $Ru-(TiO_2)_6$  cluster, which is sufficiently large to study the nitrogen reduction mechanism. To enhance nitrogen activation, the number of Ru atoms was increased to three atoms loaded on the  $(TiO_2)_6$  cluster. In this study, the  $Ru_3-(TiO_2)_6$  cluster is selected as a promising photocatalyst to investigate the photocatalytic nitrogen reduction mechanism. The model used is adapted from our previous work,<sup>[15]</sup> where the stability of  $(TiO_2)_n$  clusters was ascertained using MD simulations.

#### 2.1.2. Adsorption

The adsorption modes of  $H_2$ ,  $N_2$ , and  $NH_3$  were calculated on the optimized structure of the  $Ru_3-(TiO_2)_6$  cluster. The isolated adsorbates were enclosed and optimized in the simulation cell, which provided at least 10  $\text{\AA}$  of vacuum in each dimension. The adsorption energies ( $E_{ads}$ ) were calculated using the following equation.

$$E_{\text{ads}} = E_{\text{cluster + adsorbed species}} - (E_{\text{cluster}} + E_{\text{isolated species}}) \quad (1)$$

where  $E_{\text{cluster + adsorbed species}}$  refers to the total energy of  $\text{H}_2$ ,  $\text{N}_2$ , or  $\text{NH}_3$  adsorbed on the cluster, respectively;  $E_{\text{cluster}}$  is the total energy of the isolated cluster; and  $E_{\text{isolated species}}$  is the total energy of isolated  $\text{H}_2$ ,  $\text{N}_2$ , or  $\text{NH}_3$ . The adsorption of H was determined relative to  $\frac{1}{2}\text{H}_2$ .

### 2.1.3. Reaction Mechanism

The nitrogen reduction mechanism was investigated in the ground and first excited states. The nitrogen dissociation mechanism was studied in detail, with each elementary step in the reaction pathway considered. All initial and final precursors, as well as the intermediates adsorbed on the clusters, were optimized individually. Transition states were determined using the nudged elastic band method.<sup>[30]</sup> After obtaining the optimized structures for each step in the dissociative reaction pathway and the corresponding transition states, the activation and reaction energies were calculated, respectively. The activation energy was calculated as

$$E_A = E_{\text{TS}} - E_R \quad (2)$$

where  $E_A$  denotes the activation energy,  $E_{\text{TS}}$  the energy of the transition state, and  $E_R$  the energy of the initial state.

The reaction energy ( $\Delta E$ ) was calculated using the following equation.

$$\Delta E = E_P - E_R \quad (3)$$

where  $E_P$  refers to the energy of the product state.

Vibrational analysis was employed to confirm that the obtained transition states contained only one imaginary frequency in the direction of the reaction, while stable intermediates contained none.

### 2.1.4. Excited State Calculations

Excited state calculations were performed using TD-DFT in the linear-response regime.<sup>[19,31]</sup> The structures optimized at the ground-state DFT level were used for the excited-state calculations without further geometry optimization. According to Kasha's rule, only the first excited state is prominent in photoemission processes.<sup>[32]</sup> Excited state calculations were carried out in a single-point approach, as the structures of each elementary step were kept optimized at the ground-state geometry due to computational constraints (TD-DFT is two to three orders of magnitude more costly than conventional DFT).

## 2.2. Microkinetic Model

### 3. Microkinetic Model

The parameters obtained using (TD-)DFT were incorporated into a microkinetic model to study the kinetics of nitrogen photoreduction and compare the TD-DFT-derived results to the ground-state ammonia synthesis, taking into account the time

evolution of the photocatalytic process.<sup>[33]</sup> The aim of this study is to demonstrate the significance of incorporating excitation effects (or executing the reaction on the excited plane) in comparison to performing DFT exclusively in the ground state, as this approach yields divergent outcomes. In this regard, the model functions as a proof of concept rather than as a representation of a specific experimental setup. In order to achieve clarity regarding the effects, a simple and easily comprehensible microkinetic model was selected.

A microkinetic model was set up with the following assumptions: 1) The reactor is considered an ideal batch reactor (recalculation to plug flow reactor is trivial, as time is substituted for position along the reactor). 2) Temperature and pressure are constant (applicable due to low conversions). 3) Mass transfer is neglected. 4) Mixing is considered ideal.

As the aim of this study is to demonstrate the differences in kinetics, which stem from the inclusion or exclusion of the excited states, a mock-up reactor was used. The factor of available active sites for gas species ( $f$ ) is calculated as<sup>[34]</sup>

$$f = \frac{N \times R \times T}{V_{\text{cat}}} \quad (4)$$

where  $N$  is the numerical density of active sites,  $R$  is the gas constant,  $T$  is the temperature, and  $V_{\text{cat}}$  is the catalyst volume. As  $f$  was varied at different temperatures,  $N/V_{\text{cat}}$  was kept constant with a ratio of 7.77:1 mol L<sup>-1</sup> m<sup>-2</sup>. The photocatalytic process was integrated into the microkinetic model using the parameters derived from DFT calculations, where the system was already in a photoactivated state. Photoactivation was therefore considered implicitly, and its effects on the reaction kinetics were modeled explicitly.

A set of differential equations was formulated and solved for all the considered gas and surface reactions using the LSODA solver<sup>[35]</sup> as part of the SciPy package in Python. The LSODA solver is situated between stiff and nonstiff methods, and thus, proved to be an optimal choice for our system. Our model uses the Langmuir–Hinshelwood kinetics,<sup>[36]</sup> with all individual active sites considered equal. Therefore, the average surface coverages are taken into account, and no gaseous reactions are presumed to take place.

Based on the already established mechanisms for ammonia production,<sup>[37]</sup> we propose the following elementary reaction equations, where asterisks denote active surface sites.





For our system, a general differential equation is written as<sup>[9]</sup>

$$\frac{dC_j}{dt} = r_j^{\text{ads}} - r_j^{\text{des}} + \sum_{j=1}^n r_j \quad (13)$$

where  $dC_j$  refers to the bulk concentration of species  $j$ , while  $r_j^{\text{ads}}$ ,  $r_j^{\text{des}}$ , and  $\sum_{j=1}^n r_j$  denote the reaction rates of adsorption, desorption, and the sum of the elementary reaction steps for the species  $j$ , respectively.

The rate equation for the adsorption of gaseous species is expressed as

$$r_j^{\text{ads}} = k_j^{\text{ads}} \cdot P_j \cdot \Theta_{\text{empty}} \quad (14)$$

where  $k_j^{\text{ads}}$  represents the forward rate coefficient,  $P_j$  denotes the partial pressure of species  $j$ , and  $\Theta_{\text{empty}}$  is the empty active site. The forward rate coefficient is calculated as

$$k_j^{\text{ads}} = \frac{P \cdot A}{\sqrt{2 \cdot \pi \cdot m_j \cdot k_B \cdot T}} \quad (15)$$

where  $P$  denotes pressure (1 bar),  $A$  the surface area per active site ( $0.1 \text{ nm}^{-2}$ ), and  $m_j$  the mass of the species  $j$ .  $k_B$  is the Boltzmann constant<sup>[38]</sup> and  $T$  the temperature.

Similarly, a rate equation for the desorption of gaseous species can be written as follows

$$r_j^{\text{des}} = k_j^{\text{des}} \cdot \Theta_j \quad (16)$$

where  $k_j^{\text{des}}$  refers to the backward rate coefficient and  $\Theta_j$  the surface coverage of species  $j$ . The rate coefficient corresponds to surface reactions.

$$k_j^{\text{des}} = \frac{k_B \cdot T}{h} \cdot e^{\frac{E_j^{\text{ads}}}{k_B \cdot T}} \quad (17)$$

where  $h$  denotes Planck's constant, and  $E_j^{\text{ads}}$  is the adsorption energy of species  $j$  (negative value for the adsorption energy by definition).

For the reactions occurring on the surface, the activation barriers occurring in the forward ( $E_{\text{for}}$ ) and backward ( $E_{\text{rev}}$ ) directions are described as

$$E_{\text{for}} = E_{\text{TS}} - E_{\text{R}} \quad (18)$$

$$E_{\text{rev}} = E_{\text{TS}} - E_{\text{P}} \quad (19)$$

where  $E_{\text{TS}}$  denotes the energy of the saddle point (transition state),  $E_{\text{R}}$  the energy of the initial state, and  $E_{\text{P}}$  the energy of the final state. Additionally, the reaction rates for surface reactions in the forward ( $k_{\text{for}}$ ) and backward ( $k_{\text{rev}}$ ) directions are described as

$$k_{\text{for}} = \frac{k_B \cdot T}{h} \cdot e^{-\frac{E_{\text{for}}}{k_B \cdot T}} \quad (20)$$

$$k_{\text{rev}} = \frac{k_B \cdot T}{h} \cdot e^{-\frac{E_{\text{rev}}}{k_B \cdot T}} \quad (21)$$

Our model considered nitrogen reduction, carried out at 775 K and a total pressure of 1.2 bar. The temperature was chosen to accurately compare the reaction in the first excited state with the ground-state nitrogen reduction, which is typically run at  $\approx 500 \text{ }^\circ\text{C}$ <sup>[1,2]</sup> (conventional HB). The ratio of the initial reactants was in the stoichiometric ratio of  $N_2:H_2 = 1:3$ . The chemical potential of the  $H^+/e^-$  pair (proton and electron activity) was approximated as the chemical potential of  $\frac{1}{2}H_2$ , that is, at constant  $T$  and  $p$ .<sup>[39]</sup> This was done in order to compare the excited-state (photocatalytic) microkinetic model and the ground-state (thermocatalytic) microkinetic model *ceteris paribus*. In effect, only the photocathode part was investigated, as  $N_2$  reduction occurs there. We neglected the readsorption of ammonia once formed, as it would poison the surface due to its strong adsorption capacity, which is irrelevant for the surface kinetics.<sup>[40]</sup>

The turnover frequency (TOF)<sup>[41]</sup> was analyzed when studying the effects of temperature and different total pressures. TOF was calculated as

$$\text{TOF} = \frac{p(\text{NH}_3)}{t \times N(\text{active sites})} \quad (22)$$

where  $p(\text{NH}_3)$  is the partial pressure of  $\text{NH}_3$ ,  $t$  is time, and  $N(\text{active sites})$  is the number of active sites, which is kept constant. When calculating the TOF for the Arrhenius plot, the ratio between  $p(\text{H}_2)$  and  $p(\text{N}_2)$  was kept at 3:1. The activation energy obtained from the Arrhenius plot is given by the following equation.

$$\ln(\text{TOF}) = \ln(A) - \frac{E_A}{R \cdot T} \quad (23)$$

where  $A$  represents the pre-exponential factor,  $E_A$  the activation energy,  $R$  is the gas constant, and  $T$  is the temperature.<sup>[42,43]</sup>

## 4. Results and Discussion

To understand the catalyst's electronic properties, static calculations on the optimized  $\text{Ru}_3-(\text{TiO}_2)_6$  cluster were performed. The density of states (DOS) and the projected DOS (PDOS) were calculated, followed by a detailed study of the adsorption modes of nitrogen ( $N_2$ ) and ammonia ( $\text{NH}_3$ ), as well as the charge transfer upon adsorption. Subsequently, the reaction mechanism was studied in the ground state (DFT) and the first excited state (TD-DFT). The obtained parameters (adsorption energies, activation barriers, and reaction energies) were cast into a first-principles-based microkinetic model, which included two scenarios: ground state and first excited state.

## 4.1. First-Principles Calculations

### 4.1.1. Electronic Properties of the $\text{Ru}_3\text{-(TiO}_2)_6$ Cluster Photocatalyst

Good catalysts for nitrogen reduction bind nitrogen moderately strongly, which allows for the dissociation of  $\text{N}_2$  on one hand, but not too strongly as to impede the formation of  $\text{NH}_x$  species. The dissociation of  $\text{N}_2$  is facilitated by a large charge transfer from the catalyst to the antibonding orbitals of  $\text{N}_2$ . In photocatalysis, the energy difference between the valence and conduction bands, known as the band gap, is also crucial, as it must correspond to the energy of the incident photons we want to use. In molecules and small clusters, these bands can be thought of as the equivalents of highest occupied molecular orbital (HOMO) and lowest unoccupied molecular orbital (LUMO) orbitals.<sup>[44]</sup> The HOMO and LUMO are useful for identifying the nucleophilic and electrophilic regions of a  $\text{Ru}_3\text{-(TiO}_2)_6$  cluster. As a fully occupied molecular orbital, the HOMO acts as a nucleophile, while the LUMO, being the LUMO, accepts electrons, and thus, acts as an electrophile, interacting with

nucleophilic regions. For our case of  $\text{Ru}_3\text{-(TiO}_2)_6$ , we visualized them in **Figure 1**.

We observe that they mostly spread over the Ru atoms, which are the catalytically active part of the catalyst. To understand the contribution of individual atoms to the overall charge density, we plot a spin-polarized PDOS relative to the Fermi level set at 0.0 eV (see **Figure 2**), calculated at the hybrid level due to known deficiencies of generalized gradient approximation (GGA) methods in describing semiconductors. We observe that Ti d orbitals make up the bulk of the lower conduction band, which is the photoactive part of the catalyst. Ruthenium d orbitals are located between oxygen p orbitals at  $\approx -2.2$  eV and titanium d orbitals at  $\approx +1.5$  eV. Our results are consistent with Zhang et al.<sup>[45]</sup> who have shown that with  $\text{Ru}_{10,20,22}$  clusters on a  $\text{TiO}_2$  (101) surface, the Ru d orbitals are also spread between the O p and Ti d orbitals.

We calculated the charge distribution in the  $\text{Ru}_3\text{-(TiO}_2)_6$  cluster using Bader charge analysis. The results indicate a total charge transfer of  $+0.48 e_0$  from the three Ru atoms to the  $\text{TiO}_2$  cluster (0.22, 0.09, and 0.17  $e_0$  per Ru atom, respectively). The observed charge transfer is consistent with the formation of

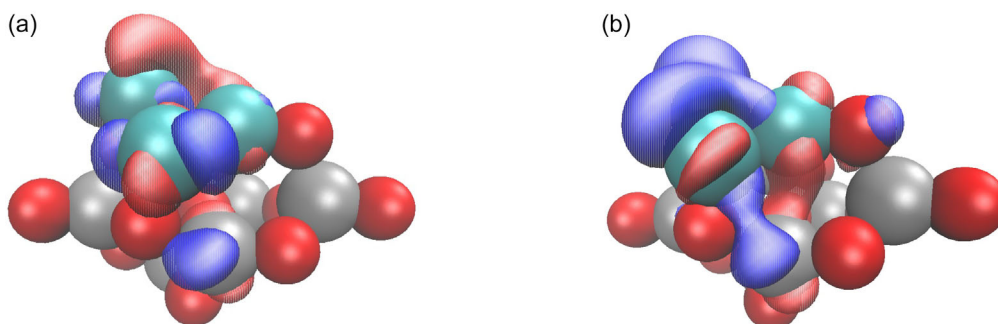


**Figure 1.** a) HOMO and b) LUMO orbitals of the  $\text{Ru}_3\text{-(TiO}_2)_6$  cluster at an isosurface of  $\pm 0.02 e_0 \text{ \AA}^{-3}$ .

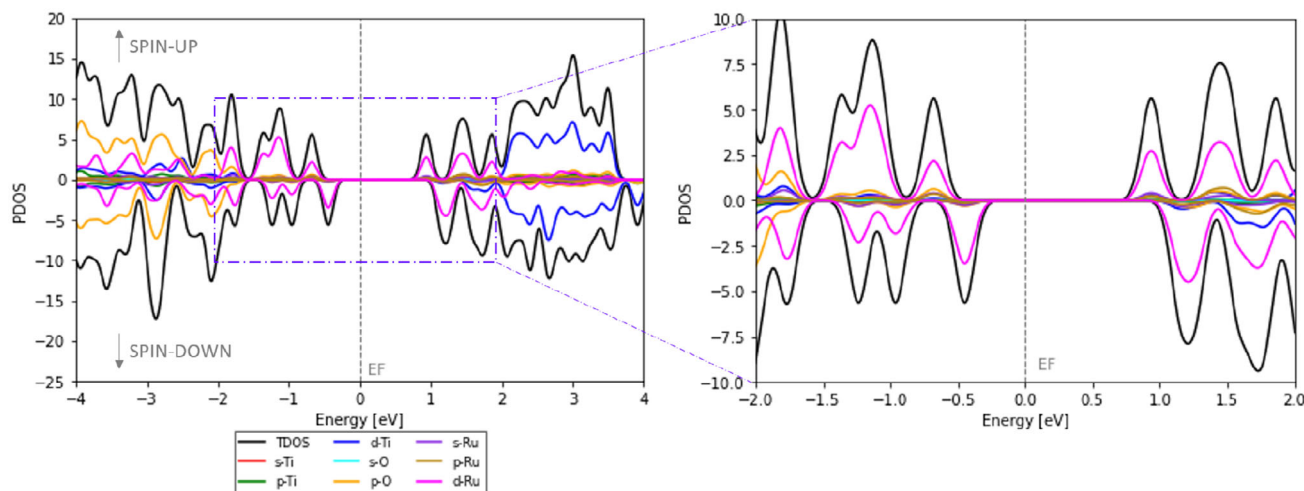


**Figure 2.** DOS and PDOS, showing the projected atomic orbital distribution per energy level, for the  $\text{Ru}_3\text{-(TiO}_2)_6$  cluster calculated using the HSE06 functional. A magnified section between  $-2$  and  $2$  eV is provided for clarity. The Fermi level is set to 0.0 eV.

Ru *d* midgap states between the O *p* and Ti *d* orbitals, as revealed by the PDOS analysis in Figure 2.

#### 4.1.2. Adsorption of Initial and Final Precursors of Nitrogen Reduction Mechanism

Adsorption of all participating species was assessed, as too strongly adsorbed reactants or products poison the catalyst,<sup>[46]</sup> while too weakly interacting species do not get activated. The most favorable adsorption modes, charge transfer, Bader charges, and bond length with bond order were calculated.

The nitrogen molecule can adsorb in either an end-on or side-on configuration, occupying one or two adsorption sites, respectively.<sup>[4,47]</sup> As shown in Figure 3, the Ru atom acts as an active site for the adsorption of N<sub>2</sub> and NH<sub>3</sub>, while the PDOS plots for the end-on and side-on adsorption of N<sub>2</sub> and NH<sub>3</sub> are given in the Supporting Information.

In the ground state, N<sub>2</sub> adsorbs more strongly in the end-on adsorption configuration (−1.45 vs. −1.02 eV for the side-on configuration). A similar effect is observed in the excited state, with the adsorption energy of −1.37 eV in the end-on configuration

and −1.05 eV in the side-on configuration. However, only the side-on configuration is conducive to activation and subsequent dissociation, as reflected by a larger elongation of its triple bond (to 1.137 Å for end-on vs. 1.191 Å for side-on) and higher charge transfer from Ru atoms to the adsorbed N<sub>2</sub> (0.30 *e*<sub>0</sub> for end-on and 0.59 *e*<sub>0</sub> for side-on configurations, respectively). In the side-on configuration, both nitrogen atoms are equally activated (charge transfer of 0.33 and 0.26 *e*<sub>0</sub> due to the asymmetry of the cluster model), while in the end-on configuration, only the nitrogen atom in contact with the surface is strongly activated (charge transfer of 0.76 *e*<sub>0</sub>).

Ammonia is adsorbed on top of a Ru atom at a distance of 2.16 Å with an interaction of −1.16 eV in the ground state and −1.30 eV in the first excited state. The adsorption energy of an H atom was calculated relative to H<sub>2</sub> and was found to be −0.08 eV in the ground state and −0.13 eV in the first excited state. It adsorbs on the Ru atom at a distance of 0.96 Å. We list the adsorption energies along with the literature data for Ru(0001) and Bader charges in Table 1 and 2, respectively.

Excitation also brings about a charge redistribution within the species. In Figure 4, we show the charge density difference

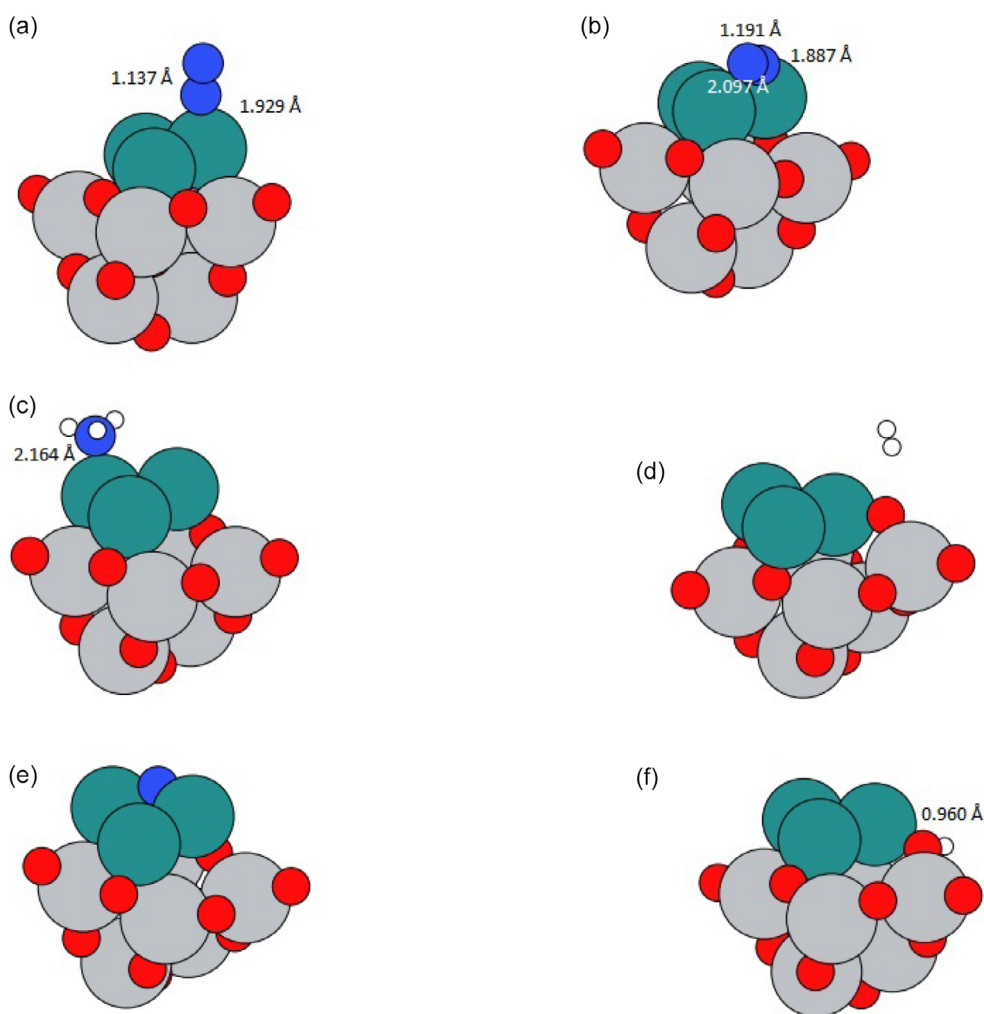


**Figure 3.** Adsorption modes of a) N<sub>2</sub> (end-on configuration), b) N<sub>2</sub> (side-on configuration), c) NH<sub>3</sub>, d) H<sub>2</sub>, e) N, and f) H on the Ru<sub>3</sub>–(TiO<sub>2</sub>)<sub>6</sub> cluster.

**Table 1.** Adsorption energies ( $E_{\text{ads}}$  of  $\text{N}_2$  (end-on and side-on adsorption configurations),  $\text{NH}_3$ ,  $\text{H}_2$ , and  $\text{H}$  on the cluster.

Adsorbates	$E_{\text{ads}}$ [eV] (ground state)	$E_{\text{ads}}$ [eV] (excited state)	Literature data on Ru(0001) (ground state)
end-on $\text{N}_2$	-1.45	-1.37	-0.74 <sup>[53]</sup>
side-on $\text{N}_2$	-1.02	-1.05	NaN
$\text{NH}_3$	-1.16	-1.30	-1.32 <sup>[50]</sup>
$\text{H}_2$	-0.05	-0.05	-0.21 (top site), -0.05 (fcc and hcp sites) <sup>[54]</sup>
$\text{H}$	-0.08	-0.13	-0.52 <sup>[50]</sup>

**Table 2.** Charge transfer calculated by the Bader charge analysis for the adsorption of  $\text{N}_2$  (end-on and side-on),  $\text{N}$ ,  $\text{NH}_3$ , and  $\text{H}_2$ .

Adsorbed species	$\Delta q$ [ $e_0$ ]
end-on $\text{N}_2$	-0.30
side-on $\text{N}_2$	-0.59
$\text{N}$	-0.76
$\text{NH}_3$	+0.14
$\text{H}_2$	0.0

between the first excited state and the ground state for the end-on and side-on adsorption of  $\text{N}_2$ , and the adsorption of  $\text{NH}_3$ .

#### 4.1.3. Reaction Mechanism

Although being a small molecule,  $\text{N}_2$  can undergo several pathways during its transformation to ammonia. In general, we speak of the dissociative or associative mechanisms, the latter being further divided into distal, alternating, and enzymatic pathways. On ruthenium-based catalysts,  $\text{N}_2$  first dissociates, followed by successive hydrogenation steps,<sup>[4,47]</sup> which is also the pathway used in this work.

The focus of our research was to study the photocatalytic nitrogen reduction reaction and compare the results with thermocatalytic ammonia synthesis.

Herein, we wish to compare the effect that accounting for or neglecting excitations has on the mechanistic description of kinetics itself. To compare these effects in the photocatalytic reaction, where hydrogen is supplied by water splitting, and to the thermocatalytic reaction, where active hydrogen stems from  $\text{H}_2$  dissociation, we focused only on the nitrogen hydrogenation part. Water splitting on  $\text{TiO}_2$  photocatalysts, however, is already a well-studied reaction.<sup>[48,49]</sup>

Each elementary step in the photocatalytic dissociation was considered individually in a way that maintains thermodynamic consistency. To account for the photocatalytic process, the mechanism was studied in the first excited state to keep the system manageable, backed up by Kasha's rule.<sup>[32]</sup> We show the potential energy surface in **Figure 5** and list the activation barriers and reaction energies in **Table 3**.

Dissociation of  $\text{N}_2$  is, alongside  $\text{NH}_2$  hydrogenation, the limiting step in ammonia production. On the  $\text{Ru}_3-(\text{TiO}_2)_6$  cluster,  $\text{N}_2$  dissociation is an exothermic process with a high barrier of 1.98 eV in the ground state, which is reduced to 1.85 eV in the excited state. Moreover, this step becomes more exothermic in the excited state, with reaction energies of -0.62 and -0.99 eV for the ground state and excited state, respectively. The dissociated nitrogen atoms are then progressively hydrogenated.

The first two hydrogenation steps (to  $\text{NH}$  and  $\text{NH}_2$ ) are exothermic and occur rapidly. The reaction energies are -0.72 eV (-0.47 eV in the excited state) and -0.62 eV (-0.98 eV in the excited state), respectively, and the reaction barriers are 1.26 eV (1.48 eV in the excited state) and 1.14 eV (0.84 eV in the excited state), respectively. It is well known<sup>[50,51]</sup> that hydrogenation of  $\text{NH}_2$  to ammonia is endothermic on ruthenium-based catalysts, which bind hydrogen very strongly. We calculate the reaction energy of 0.39 eV (0.25 eV in the excited state) and an activation barrier of 1.37 eV (1.45 eV in the excited state).

Comparable results for the ground state mechanism have been reported for Ru(0001), for example by Logad'ottir et al. who found the highest activation barrier of 1.9 eV over the terraces of Ru(0001) for nitrogen dissociation.<sup>[50]</sup>

During photocatalysis, the reaction predominantly occurs on the excited-state electronic plane. In addition to the conventional view that incident light excites the electrons in the catalyst with the adsorbed nitrogen molecule, which activates it, we show that

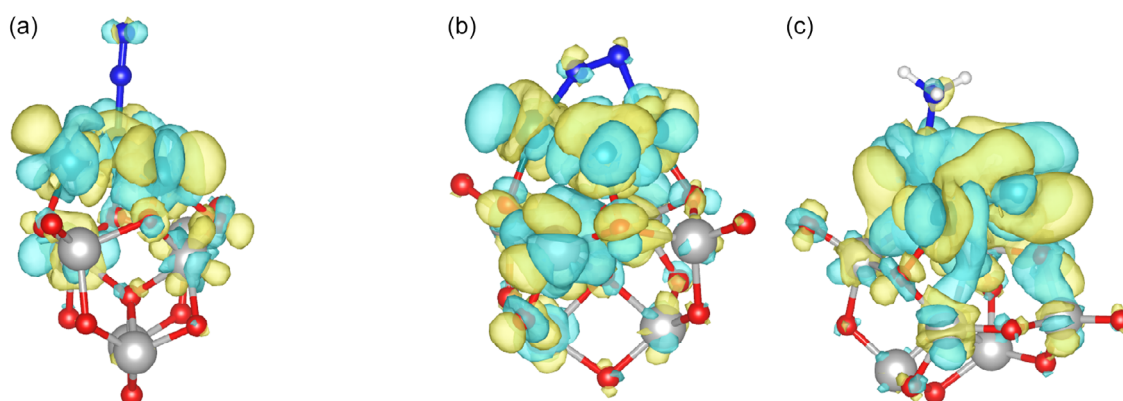


**Figure 4.** Charge density difference between the first excited state and the ground state adsorption of a)  $\text{N}_2$  (end-on), b)  $\text{N}_2$  (side-on), and c)  $\text{NH}_3$  on the  $\text{Ru}_3-(\text{TiO}_2)_6$  cluster at an isovalue of  $+0.001 e_0 \text{ \AA}^{-3}$  (yellow color) and  $-0.001 e_0 \text{ \AA}^{-3}$  (blue color).

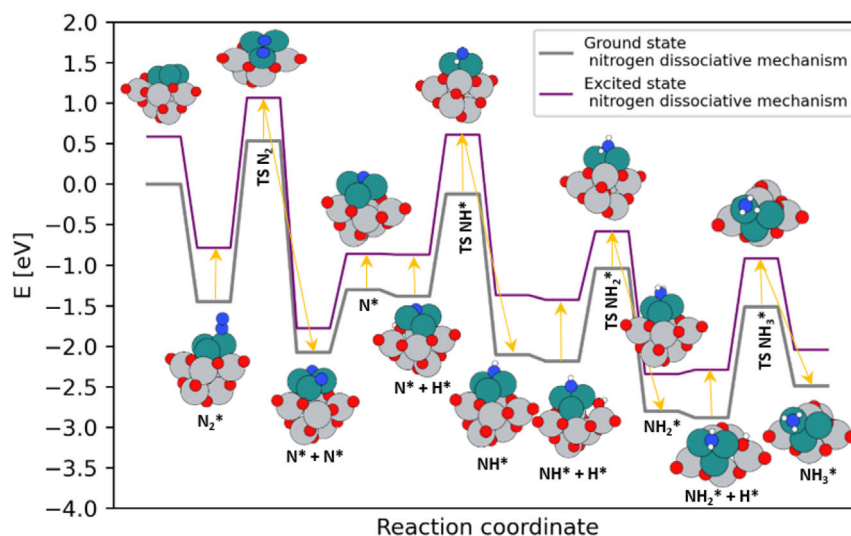


Figure 5. Nitrogen dissociative reduction mechanism in the ground state and the first excited state over  $\text{Ru}_3\text{-(TiO}_2)_6$ .

Table 3. The activation ( $E_a$ ) and reaction energies ( $\Delta E$ ) of elementary steps for the ground state and the first excited state ammonia synthesis.<sup>[50]</sup>

Individual step	$E_a$ [eV] (the ground state)	$E_a$ [eV] on Ru(0001) <sup>[50]</sup>	$E_a$ [eV] (excited state)	$\Delta E$ [eV] ground state	$\Delta E$ [eV] (excited state)
$\text{H} + \text{H} \rightleftharpoons \text{H}_2$	0.64	n/a	0.65	0.11	0.21
$\text{N}_2 \rightleftharpoons 2\text{N}$	1.98	1.9	1.85	-0.62	-0.99
$\text{N} + \text{H} \rightleftharpoons \text{NH}$	1.26	1.2	1.48	-0.72	-0.47
$\text{NH} + \text{H} \rightleftharpoons \text{NH}_2$	1.14	1.3	0.84	-0.62	-0.98
$\text{NH}_2 + \text{H} \rightarrow \text{NH}_3$	1.37	1.4	1.45	0.39	0.25

the entire reaction mechanism exhibits altered kinetics. In addition to the decrease in the barrier for  $\text{N}_2$  dissociation, other steps are also generally accelerated due to lower barriers and improved exothermicity.

The barrier for the dissociation of a nitrogen molecule is found to be 0.14 eV lower, and the reaction energy is 0.37 eV more exothermic in the excited state than in the ground state. The first hydrogenation is slightly slower than in the ground state, with a 0.25 eV higher energy barrier, while the second hydrogenation has a 0.3 eV lower activation energy in the excited state. None of these steps are rate-limiting. The last hydrogenation has only a slightly higher activation barrier (0.08 eV).

Based on the excitation energy of the  $\text{Ru}_3\text{-(TiO}_2)_6$  cluster, the corresponding absorption wavelength falls within the infrared region,  $\approx 2.12 \mu\text{m}$ . This low-energy absorption limits the cluster's ability to effectively utilize visible light, contributing to increased charge carrier recombination and reduced photocatalytic efficiency. To overcome this limitation, we suggest maintaining the number of Ru atoms while increasing the size of the  $\text{TiO}_6$  cluster. This approach is expected to enable absorption at shorter wavelengths, enhancing light utilization and potentially improving catalytic performance. However, these modifications are beyond the scope of the present study, as our primary aim was to demonstrate the beneficial effect of excited-state calculations on the nitrogen reduction mechanism.

## 4.2. Microkinetic Modeling

To study the kinetics of photocatalytic ammonia synthesis, a first-principles microkinetic model was constructed using the parameters obtained from our DFT calculations. As discussed earlier, we focused on studying nitrogen reduction, while active hydrogen is assumed to form from water splitting, which was not modeled explicitly. In all instances, we compare the ground-state and excited-state regimes under the same conditions.

In Figure 6, we show the results of a microkinetic model for ground-state and excited-state ammonia production. Upon cursory inspection, we observe very little difference, and the reaction seems to follow the same mechanism. A closer look, however, reveals a quantitative difference. In the excited state, the reaction is faster, and surface coverages are thus different. There is virtually no NH and  $\text{NH}_2$  present, as they react more quickly. Due to facilitated  $\text{N}_2$  dissociation, the surface concentration of N is increased.

Possible changes in the mechanism and exact kinetic effects were evaluated via the TOF and its dependence on temperature. In Figure 7, we show the Arrhenius plot for the ground-state and excited-state scenarios. The calculated apparent activation barrier for  $\text{NH}_3$  production is 0.14 eV lower (1.84 vs. 1.98 eV) in the excited state, which corresponds to approximately an order of magnitude increase in the reaction rate. Dahl et al. also reported high activation energy determined from TOF when ammonia

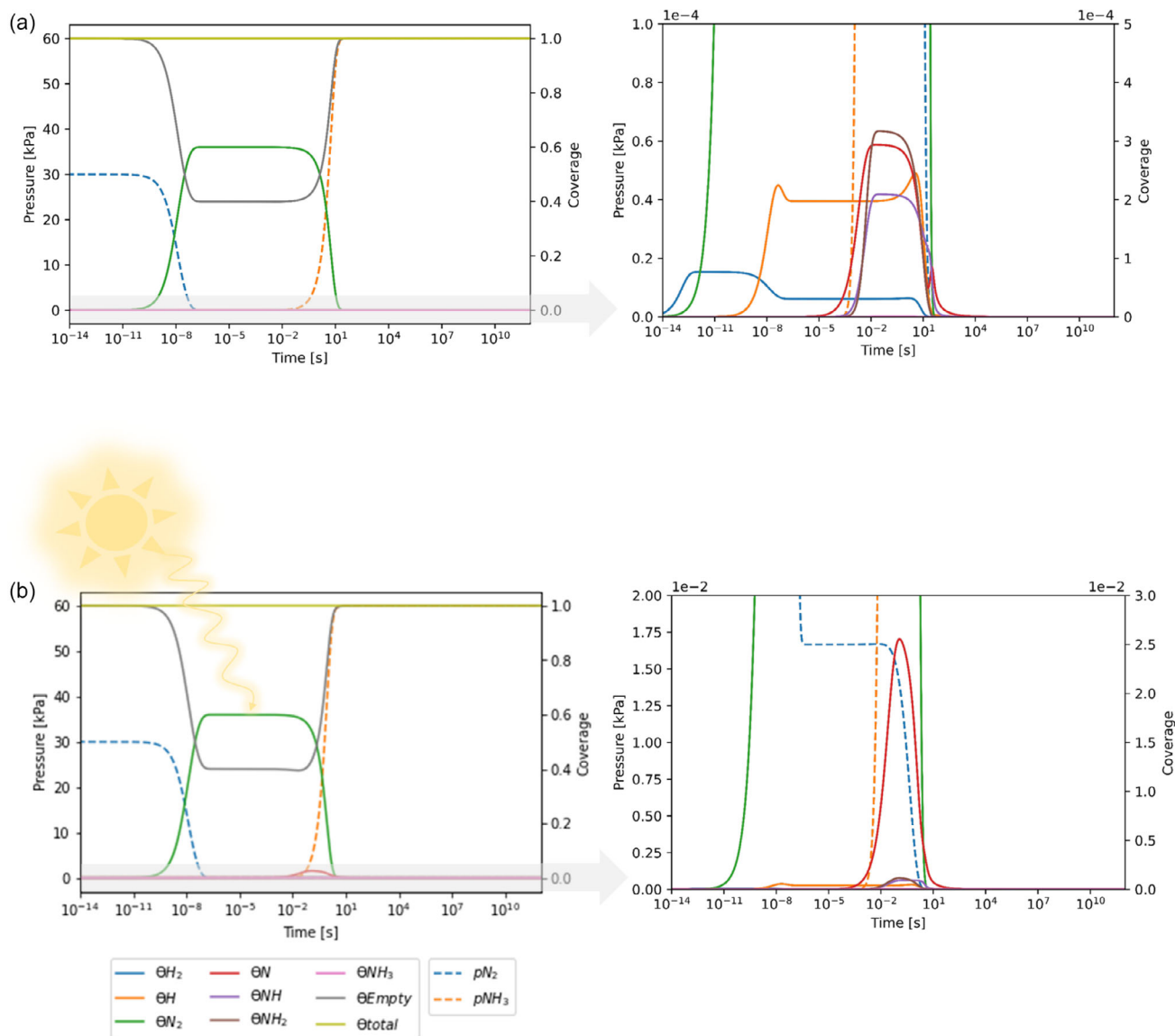


**Figure 6.** The temporal evolution in a) (left) the ground state and b) (left) the first excited state nitrogen reduction over  $Ru_3-(TiO_2)_6$  cluster at a temperature of 775 K. Zoomed pressure range and coverage of the temporal evolution in a) (right) the ground state and b) (right) the first excited state nitrogen reduction over  $Ru_3-(TiO_2)_6$  cluster.

synthesis was studied over the  $Ru(0001)$  catalyst.<sup>[52]</sup> They suggested that the activation energy for nitrogen dissociation be decreased, as it was found to be the rate-determining step.

Furthermore, we studied the reaction order with respect to varying reactant composition ( $p[H_2]$  and  $p[N_2]$ ). In **Figure 8**, we show the dependance on the composition at a constant total pressure of 1.2 bar. The maximum TOF in the ground state is observed at an  $N_2:H_2$  ratio of 1:2.64, while in the excited state, the peak shifts to 1:3.80.

## 5. Conclusion

Photocatalytic ammonia synthesis has garnered considerable attention in the attempt to overcome the shortcomings of the

conventional HB process. While there have been several successful experimental implementations, theoretical modeling lags behind. Excited states are only accounted for in the calculations of electronic properties, while mechanisms and kinetics are usually studied at the ground state level with conventional DFT. Herein, we show that this is insufficient, as demonstrated by the example of the  $Ru_3-(TiO_2)_6$  photocatalyst. We modeled the reaction using ab initio TD-DFT, and the results were subsequently used in a microkinetic model.

First, we investigated the electronic properties of the  $Ru_3-(TiO_2)_6$  cluster. The band gap was approximated as the energy difference between the HOMO and LUMO orbitals, which is strongly dependent on the number of Ru atoms and ranged from 2.38 eV for the  $Ru-(TiO_2)_6$  cluster<sup>[15]</sup> to 0.81 eV for the  $Ru_3-(TiO_2)_6$  cluster. The DOS analysis demonstrated that

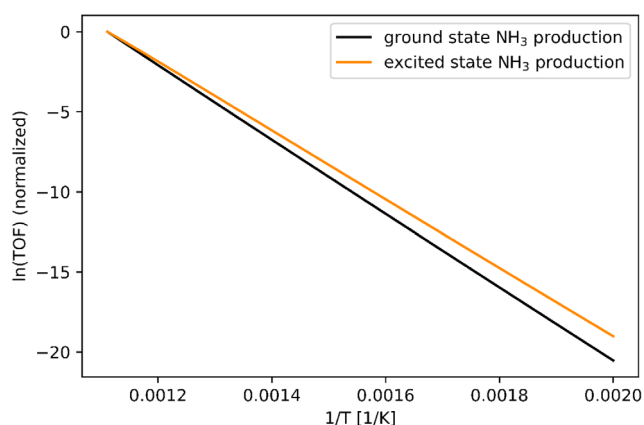


**Figure 7.** TOF for the ground state and excited state  $\text{NH}_3$  production over  $\text{Ru}_3\text{-(TiO}_2)_6$  cluster with varying temperature.

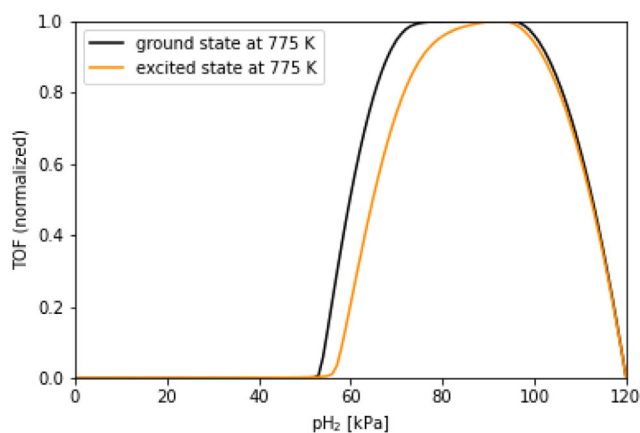


**Figure 8.** TOF for the ground state and excited state  $\text{NH}_3$  production over  $\text{Ru}_3\text{-(TiO}_2)_6$  cluster calculated at a temperature of 775 K for varying  $\text{pH}_2$ .

Ru d-orbitals fit between O p-orbitals located below the Fermi level and Ti d-orbitals located above the Fermi level.

Subsequently, the adsorption and reaction mechanisms were studied. While  $\text{N}_2$  adsorption is strongest in the end-on orientation, it requires the side-on orientation for dissociation to proceed. There, a larger charge transfer activates the molecule. The reaction mechanism, which consists of  $\text{N}_2$  dissociation and subsequent stepwise hydrogenations of N, NH, and  $\text{NH}_2$ , remains the same in the excited state, but the barriers and energetics change. In all instances,  $\text{N}_2$  dissociation remains the rate-determining step. Its activation barrier is decreased from 1.98 to 1.85 eV upon excitation.

Microkinetic modeling provided a quantitative measure of the difference between the excited-state and ground-state scenarios. At all temperatures, the reaction rate is faster under photocatalytic conditions. The apparent activation barrier, as obtained from the Arrhenius plot, is  $E_a = 1.84$  eV in the excited state and 1.98 eV in the ground state calculation. Lastly, the effect of the reactant ratio was investigated. In the ground state, the maximum reaction rate is observed at an  $\text{N}_2\text{:H}_2$  ratio of 1:2.64. In the excited state, this changes to 1:3.80.

Since GGA functionals poorly describe electronic properties of semiconductors, such as  $\text{TiO}_2$ , electronic properties were computed using a hybrid functional (HSE06). However, for structural optimizations and TD-DFT calculations, only a GGA approach was computationally feasible. To compensate for its known pitfalls, the D3 empirical dispersion and Hubbard U correction were included.

To the best of our knowledge, this is the first study to model ammonia synthesis in the photocatalytic regime. We have shown that the reaction rate is changed not only due to the promotion of the catalyst, but that all the reaction steps have different kinetic parameters. Furthermore, linking TD-DFT calculations with microkinetic modeling extends the understanding of photocatalytic ammonia synthesis to the macroscale. This computational approach is transferable to other photocatalytic reactions, making it a versatile tool for future theoretical photocatalysis research.

## Supporting Information

Supporting Information is available from the Wiley Online Library or from the author.

## Acknowledgements

The authors acknowledge the Slovenian Research and Innovation Agency (ARIS) for funding. T.Ž. appreciates core funding P1-0418 and project funding J7-4636. B.L. was funded by core funding P2-0152 and project funding N2-0291. M.H. received infrastructure funding I0-0039 and project funding N1-0303. The European Commission is acknowledged for funding the Horizon EU project Dare2X (grant no. 101083905). The research was (co-)funded under the HyBReED project, supported by the European Union – NextGenerationEU. Computational resources were provided by the HPC RIVR consortium and EuroHPC JU at the HPC system Vega at the Institute of Information Science, Maribor, Slovenia.

## Conflict of Interest

The authors declare no conflict of interest.

## Author Contributions

**Taja Žibert:** data curation, formal analysis, investigation, visualization, writing—original draft. **Blaž Likozar:** funding acquisition, conceptualization, project administration, writing—review and editing. **Matej Huš:** conceptualization, methodology, supervision, writing—review and editing.

## Data Availability Statement

The data that support the findings of this study are available from the corresponding author upon reasonable request.

## Keywords

excited states, microkinetics, nitrogen reduction, photocatalysis, time-dependent density functional theory

Received: April 8, 2025

Revised: May 30, 2025

Published online:

- [1] A. E. Yüzbaşıoğlu, C. Avşar, A. O. Gezerman, *Curr. Res. Green Sustainable Chem.* **2022**, *5*, 100307.
- [2] J. W. Erisman, M. A. Sutton, J. Galloway, Z. Klimont, W. Winiwarter, *Nat. Geosci.* **2008**, *1*, 636.
- [3] M. Li, H. Huang, J. Low, C. Gao, R. Long, Y. Xiong, *Small Methods* **2018**, *3*, 1800388.
- [4] T. Žibert, B. Likozar, M. Huš, *ChemSusChem* **2024**, *17*, e202301730.
- [5] Ž. Kovačič, B. Likozar, M. Huš, *ACS Catal.* **2020**, *10*, 14984.
- [6] I. Ali, M. Suhail, Z. A. Allothman, A. Alwarthan, *RSC Adv.* **2018**, *8*, 30125.
- [7] M. Ni, M. K. Leung, D. Y. Leung, K. Sumathy, *Renewable Sustainable Energy Rev.* **2007**, *11*, 401.
- [8] A. Fujishima, K. Honda, *Nature* **1972**, *238*, 37.
- [9] Ž. Kovačič, B. Likozar, M. Huš, *Chem. Eng. J.* **2024**, *485*, 149894.
- [10] R. B. Wang, S. Körbel, S. Saha, S. Botti, N. V. Skorodumova, *J. Phys. Chem. C* **2017**, *121*, 9528.
- [11] X. Niu, D. Sun, L. Shi, X. Bai, Q. Li, X. Li, J. Wang, *J. Mater. Chem. A* **2021**, *9*, 6214.
- [12] X. Niu, A. Shi, D. Sun, S. Xiao, T. Zhang, Z. Zhou, X. Li, J. Wang, *ACS Catal.* **2021**, *11*, 14058.
- [13] Q. Zheng, W. Chu, C. Zhao, L. Zhang, H. Guo, Y. Wang, X. Jiang, J. Zhao, *WIREs Comput. Mol. Sci.* **2019**, *9*, e411.
- [14] C. F. Craig, W. R. Duncan, O. V. Prezhdo, *Phys. Rev. Lett.* **2005**, *95*, 163001.
- [15] T. Žibert, B. Likozar, M. Huš, *Fuel* **2023**, *334*, 126451.
- [16] M. Ismael, *New J. Chem.* **2019**, *43*, 9596.
- [17] L. Valenzuela, J. Ivanez, N. Keller, *Catal. Today* **2024**, *435*, 114723.
- [18] J. J. Mortensen, L. B. Hansen, K. W. Jacobsen, *Phys. Rev. B* **2005**, *71*, 035109.
- [19] J. Enkovaara, C. Rostgaard, J. J. Mortensen, J. Chen, M. Duřak, L. Ferrighi, J. Gavnholt, C. Glinsvad, V. Haikola, H. A. Hansen, H. H. Kristoffersen, M. Kuisma, A. H. Larsen, L. Lehtovaara, M. Ljungberg, O. Lopez-Acevedo, P. G. Moses, J. Ojanen, T. Olsen, V. Petzold, N. A. Romero, J. Stausholm-Møller, M. Strange, G. A. Tritsarlis, M. Vanin, M. Walter, B. Hammer, H. Häkkinen, G. K. H. Madsen, et al., *J. Phys.: Condens. Matter* **2010**, *22*, 253202.
- [20] J. P. Perdew, K. Burke, M. Ernzerhof, *Phys. Rev. Lett.* **1996**, *77*, 3865.
- [21] P. E. Blöchl, *Phys. Rev. B* **1994**, *50*, 17953.
- [22] M. Ernzerhof, G. E. Scuseria, *J. Chem. Phys.* **1999**, *110*, 5029.
- [23] J. Heyd, G. E. Scuseria, *J. Chem. Phys.* **2004**, *121*, 1187.
- [24] S. Grimme, J. Antony, S. Ehrlich, H. Krieg, *J. Chem. Phys.* **2010**, *132*, 154104.
- [25] J. Hubbard, *Proc. R. Soc. London Ser. A* **1963**, *276*, 238.
- [26] K. Chen, C. Chen, X. Ren, A. Alsaedi, T. Hayat, *Chem. Eng. J.* **2019**, *359*, 944.
- [27] X. Lin, Y. Yoon, N. G. Petrik, Z. Li, Z.-T. Wang, V.-A. Glezakou, B. D. Kay, I. Lyubinetsky, G. A. Kimmel, R. Rousseau, Z. Dohnálek, *J. Phys. Chem. C* **2012**, *116*, 26322.
- [28] D. R. Eddy, M. D. Permana, L. K. Sakti, G. A. N. Sheha, Solihudin, S. Hidayat, T. Takei, N. Kumada, I. Rahayu, *Nanomaterials* **2023**, *13*, 704.
- [29] A. M. Doyle, S. K. Shaikhutdinov, S. D. Jackson, H. Freund, *Angew. Chem. Int. Ed.* **2003**, *42*, 5240.
- [30] G. Henkelman, B. P. Uberuaga, H. Jónsson, *J. Chem. Phys.* **2000**, *113*, 9901.
- [31] C. Adamo, D. Jacquemin, *Chem. Soc. Rev.* **2013**, *42*, 845.
- [32] X. Zhang, C. Chen, W. Zhang, N. Yin, B. Yuan, G. Zhuang, X.-Y. Wang, P. Du, *Nat. Commun.* **2024**, *15*, 2684.
- [33] R. J. Rama, A. Nova, M. C. Nicasio, *ChemCatChem* **2024**, *16*, e202400224.
- [34] L. Skubic, D. Kopač, B. Likozar, M. Huš, *Appl. Surf. Sci.* **2022**, *601*, 154135.
- [35] L. Petzold, *SIAM J. Sci. Stat. Comput.* **1983**, *4*, 136.
- [36] R. J. Baxter, P. Hu, *J. Chem. Phys.* **2002**, *116*, 4379.
- [37] G. R. Wittreich, K. Alexopoulos, D. G. Vlachos, *Handbook of Materials Modeling* (Eds: W. Andreoni, S. Yip), Springer, Cham **2020**, pp. 1377-1404.
- [38] A. Bjelajac, D. Kopač, A. Fecant, E. Tavernier, R. Petrović, B. Likozar, D. Janačković, *Catal. Sci. Technol.* **2020**, *10*, 1688.
- [39] H. C. Nguyën, F. A. Garcés-Pineda, M. de Fez-Febré, J. R. Galán-Mascarós, N. López, *Chem. Sci.* **2020**, *11*, 2464.
- [40] M. El-Shafie, *Int. J. Hydrogen Energy* **2023**, *48*, 35938.
- [41] S. Kozuch, J. M. L. Martin, *ACS Catal.* **2012**, *2*, 2787.
- [42] I. W. M. Smith, *Chem. Soc. Rev.* **2008**, *37*, 812.
- [43] J. Kohout, *Molecules* **2021**, *26*, 7162.
- [44] X. Jing, Z. Zhang, T. Chen, J. Luo, *Energy Technol.* **2023**, *11*, 2201005.
- [45] S.-T. Zhang, C.-M. Li, H. Yan, M. Wei, D. G. Evans, X. Duan, *J. Phys. Chem. C* **2014**, *118*, 3514.
- [46] A. J. Medford, A. Vojvodic, J. S. Hummelshøj, J. Voss, F. Abild-Pedersen, F. Studt, T. Bligaard, A. Nilsson, J. K. Nørskov, *J. Catal.* **2015**, *328*, 36.
- [47] K. Ithisuphalap, H. Zhang, L. Guo, Q. Yang, H. Yang, G. Wu, *Small Methods* **2018**, *3*, 1800352.
- [48] E. Berardo, M. A. Zwijnenburg, *J. Phys. Chem. C* **2015**, *119*, 13384.
- [49] Y.-P. Lin, I. Isakoviča, A. Gopejenko, A. Ivanova, A. Začinskis, R. I. Eglitis, P. N. D'yachkov, S. Piskunov, *Nanomaterials* **2021**, *11*, 2900.
- [50] Á. Logadóttir, J. Nørskov, *J. Catal.* **2003**, *220*, 273.
- [51] A. Ishikawa, T. Doi, H. Nakai, *J. Catal.* **2018**, *357*, 213.
- [52] S. Dahl, J. Sehested, C. Jacobsen, E. Tornqvist, I. Chorkendorff, *J. Catal.* **2000**, *192*, 391.
- [53] J. A. Herron, S. Tonelli, M. Mavrikakis, *Surf. Sci.* **2013**, *614*, 64.
- [54] M. Puisto, H. Nenonen, A. Puisto, M. Alatalo, *Eur. Phys. J. B* **2013**, *86*, 396.